

Impact of *Lanice conchilega* on seafloor microtopography off the island of Sylt (German Bight, SE North Sea)

M. Schönke^{1,2} · P. Feldens^{1,2} · D. Wilken² · S. Papenmeier³ · C. Heinrich⁴ · J. Schneider von Deimling² · P. Held² · S. Krastel²

Received: 30 September 2016 / Accepted: 4 December 2016 / Published online: 15 December 2016
© Springer-Verlag Berlin Heidelberg 2016

Abstract This study presents a new in situ method to explore the impact of macrofauna on seafloor microtopography and corresponding microroughness based on underwater laser line scanning. The local microtopography was determined with mm-level accuracy at three stations colonised by the tubeworm *Lanice conchilega* offshore of the island of Sylt in the German Bight (south-eastern North Sea), covering approximately 0.5 m² each. Ground truthing was done using underwater video data. Two stations were populated by tubeworm colonies of different population densities, and one station had a hydrodynamically rippled seafloor. Tubeworms caused an increased skewness of the microtopography height distribution and an increased root mean square roughness at short spatial wavelengths compared with hydrodynamic bedforms. Spectral analysis of the 2D Fourier transformed microtopography showed that the roughness magnitude increased at spatial wavelengths between 0.020 and 0.003 m independently of the tubeworm density. This effect was not detected by commonly used 1D roughness profiles but required consideration of the complete spectrum. Overall, the

results reveal that new indicator variables for benthic organisms may be developed based on microtopographic data. An example demonstrates the use of local slope and skewness to detect tubeworms in the measured digital elevation model.

Introduction

Habitat mapping by remote sensing has become an important issue in the investigation and classification of the seafloor. The need for detailed habitat maps has been recognised in major initiatives that aim to enhance the environmental status of marine habitats in territorial waters (e.g. the European Marine Strategy Framework Directive, European Parliament and European Council 2008). Such maps are important for spatial planning purposes to minimize the impact exerted on habitats by increasing use of shallow water areas for activities such as tourism, fishing, resource extraction or, more recently, the installation of alternative energy infrastructures.

Currently, the monitoring of seafloor fauna, including benthic communities, is mainly achieved using optical imaging systems and sample retrieval, whereas seafloor classification is dominated by acoustic methods (Anderson et al. 2008; Brown et al. 2011). The monitoring of seafloor fauna by remote sensing would be far more efficient compared with traditional methods and is thus considered an important part of future research (Brown and Collier 2008; Anderson et al. 2008; Che et al. 2012). In addition to the need for improved classification algorithms, which is continuously being addressed (Coggan and Diesing 2011; Diesing et al. 2014; Diesing and Stephens 2015), one important reason for the difficult identification and monitoring of benthic fauna using remote sensing data is that the impact of benthic organisms on physical seafloor parameters and the signatures of remote sensing methods is poorly known.

✉ M. Schönke
mischa.schoenke@io-warnemuende.de

¹ Leibniz Institute for Baltic Sea Research Warnemünde, Seestrasse 15, 18119 Warnemünde, Germany

² Institute of Geosciences, Kiel University, Otto Hahn Platz 1, 24118 Kiel, Germany

³ Helmholtz Centre for Polar and Marine Research, Alfred Wegener Institute, Wadden Sea Station Sylt, Hafenstrasse 43, 25992 List auf Sylt, Germany

⁴ Landesamt für Landwirtschaft, Umwelt und ländliche Räume, des Landes Schleswig-Holstein, Hamburger Chaussee 25, 24220 Flintbek, Germany

Among these parameters, seafloor microtopography at the cm to mm scale has been poorly investigated, although it is a basic parameter of high importance for acoustic scatter as well as a potentially independent indicator variable for habitat mapping. While the use of morphological parameters on a larger scale is widespread in seafloor classification (Brown and Collier 2008; Brown et al. 2011), very few case studies have determined if micro-bathymetry and small-scale seafloor roughness are suitable parameters for classification or monitoring purposes, an exception being Maki et al. (2011). Currently, the measurement of fine-scale seafloor roughness requires mostly stationary, high-resolution digital elevation models with small footprints that optical systems, such as stereo photography and laser line scanners, can deliver. Although hydrodynamic bedforms have been investigated using 2D spectral analysis (Lefebvre et al. 2011, 2013), only few measurements have been reported for biological seafloor habitats or bioturbated sediments (Pouliquen and Lyons 2002; Wang and Tang 2012) because of the difficulties of measuring biologic seafloors in situ with sub-cm accuracy.

Within this context, the objective of this study was to use underwater laser line scanning to measure seafloor microtopography with mm-scale accuracy at three sites offshore of the island of Sylt in the German Bight of the south-eastern North Sea. The data were collected in August 2015 at hydrodynamically and biologically impacted seafloor sites. The impact of benthic organisms on the microtopography is assessed based on example data from sites colonised by the tube-dwelling annelid *Lanice conchilega*.

Regional setting

The study area was located 2.7 km offshore of Sylt in the German Bight (Fig. 1) at a water depth of approximately 10 m. The tide is semi-diurnal with a mean tidal range of 1.8–2.2 m (Tillmann and Wunderlich 2011), and the region is exposed to storms from the west. Several studies have described the seafloor facies in the study area based on extensive hydroacoustic surveys (Zeiler et al. 2000; Diesing et al. 2006; Markert et al. 2013; Mielck et al. 2015). The seafloor mostly comprises fine sand and E–W directed sorted bedforms composed of coarse sand. The first mode of the sorted bedform grain size distribution in the study area is between 0.25 and 0.5 mm, corresponding to medium sand (Mielck et al. 2015). Adjacent areas are composed of fine sand with first modes between 0.125 and 0.25 mm (Mielck et al. 2015). The dominating macrobenthic species in the fine sand areas is *L. conchilega* (Armonies 2000).

Materials and methods

Hardware

A ULS-200 blue (750 nm wavelength) laser line scanner manufactured by 2G Robotics (Waterloo, Ontario, Canada) was attached to a stationary lander that operates autonomously on the seafloor (Fig. 2a). In contrast to a previous laser line scanner used to measure seafloor bathymetry that moved along a translational rail across a frame (Moore and Jaffe 2002), the ULS-200 remains translationally fixed and uses a rotating laser head to capture a 3D image. A GoPro underwater video camera mounted on the lander provided continuous visual ground truthing.

The laser system scans a swath with a fixed opening angle of 50° (Fig. 2b). Along the laser footprint, the positions of 480 equidistant points are measured parallel to the Z direction. The resolution along the Y axis depends on the step size of the rotating scanner head, whereas the angular resolution along the Z axis is fixed at 0.1042°. With the laser head situated approximately 60 cm above the seafloor and a chosen angular resolution of 0.0900° along the Y axis, the settings provide a resolution in the Y and Z directions of least 1.7 mm. The range resolution along the X axis (elevation) is generally better than 0.2 mm for this application.

The ULS-200 system has several user controllable parameters that impact bottom detection. Because no experience with measuring seafloor morphology using such a laser line scanner was available, each station was measured with all sensible parameter combinations. The settings finally chosen that caused the least number of outliers due to suspension in the water column are reported in Table 1.

Data processing

The reliable removal of artificial elevation spikes/outliers due to false bottom detection is crucial for correct determination of amplitude and spectral parameters (Leys et al. 2013). For the purpose of the present study, all elevation values outside a 3 σ confidence interval around a mean are defined as outliers. A two-step filter process was applied because the standard deviation and the mean are strongly affected by those outliers, which are caused by suspension close to the laser detector. The first filter eliminates the extreme spikes, and the second filter identifies outliers closer to the seafloor surface. The two-step filter process (Fig. 3) is outlined as follows.

A smoothed surface was created by applying a 2D moving median filter with a window size of 0.018 \times 0.018 m. The smoothed surface was subtracted from the input surface. Extreme outliers were then detected by calculating the standard deviation and the

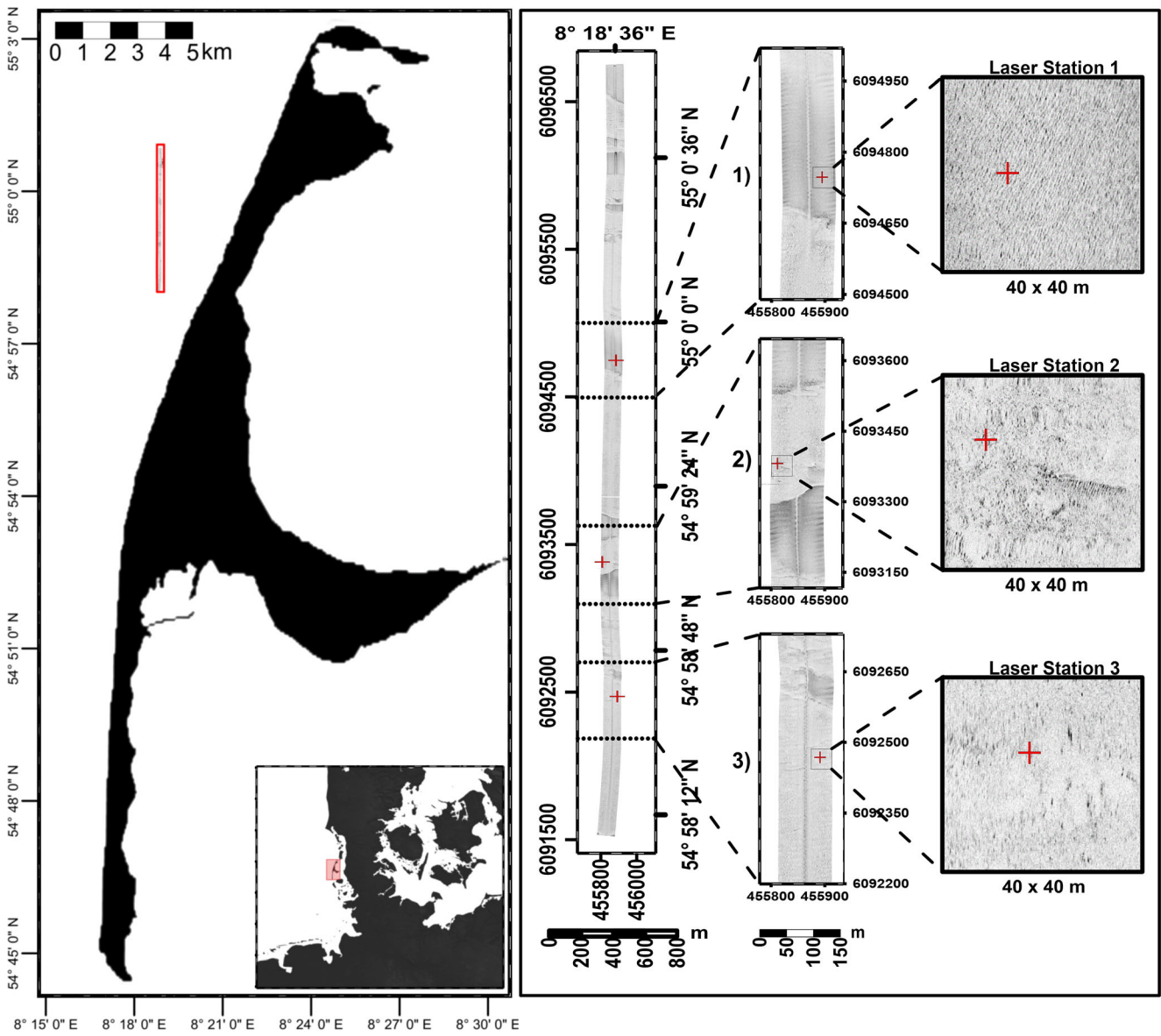


Fig. 1 Location of the research site offshore of the island of Sylt (German Bight, North Sea). *Red crosses* Locations for underwater laser line scanner stations, selected on the basis of the shown side scan sonar profile

mean of the entire subtracted surface. All values outside a 3σ confidence interval were replaced by the corresponding values of the smoothed surface (Fig. 3), and the resulting surface was used as the input for the second spike filter.

The identification of outliers located closer to the seafloor was more difficult because of the reduced variance between the outliers and actual topographic features such as tubeworms. However, compared with real topographic features, individual spikes covered a much lower area of the seafloor. A small window size for the moving median filter of 0.009×0.009 m was found to track most of the spikes while retaining the macrobenthic structures when subtracting the smoothed surface (Fig. 3). In contrast to

the first filter, the mean and standard deviation were calculated for each individual data trace to increase the sensitivity. All tracked values outside a 3σ confidence interval were replaced by corresponding values of the smoothed surface. In total, the two-step spike filter tracked and interpolated less than 2% of the data points at all stations.

To account for an eventual non-horizontal placement of the scanner frame, the data were detrended by subtracting a layer characterized by the best linear fit to the Y–X and Z–X axes. Finally, the data were normalized to a zero mean. The resulting final surface $S(y,z)$ with a resolution of 0.0018 m along the Y and Z axes was used for the calculation of statistical parameters.

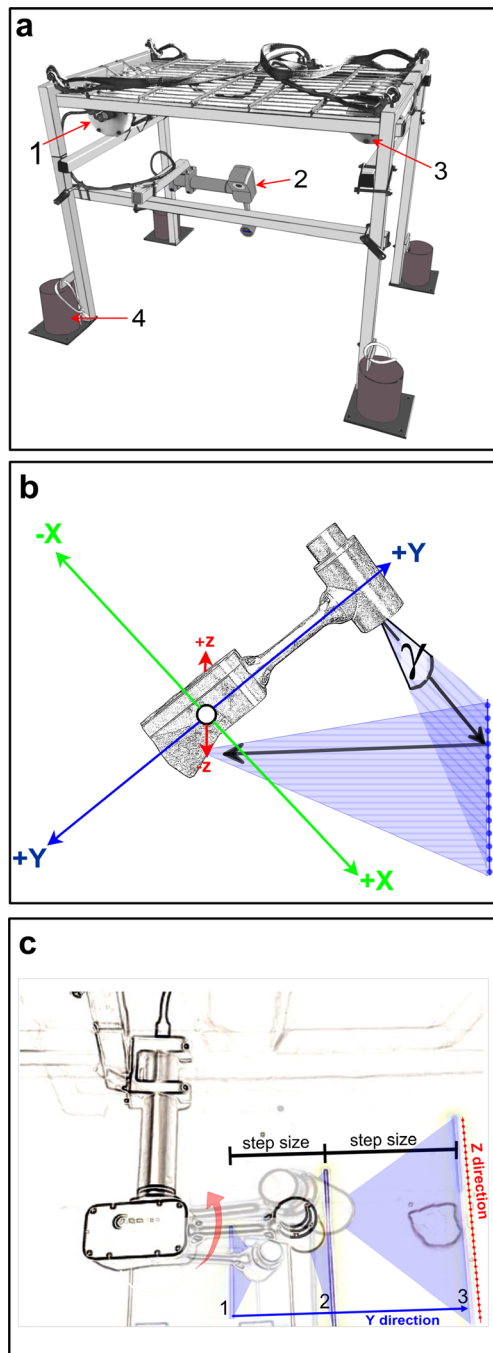


Fig. 2 **a** Schematic overview of the underwater laser line scanner system: 1 acquisition hardware, 2 laser scanner, 3 power supply, 4 stabilization weights. **b** Coordinate system conventions of the ULS-200. **c** Laser rotation process

Amplitude parameters

The root mean square roughness S_q and the surface skewness S_{sk} were calculated directly from the digital elevation model (Bhushan 2001). For data with a zero mean, the standard deviation of the elevation distribution of the scanned area corresponds to S_q :

Table 1 Settings chosen for laser measurements in turbid water offshore of Sylt

ULS-200 Setting	Value	ULS-200 Setting	Value
Minimum range	0.12 m	Filtering samples	10
Maximum range	1.5 m	Filtering proximity tolerance	64
Step size	0.09°	Filtering samples within tolerance	5
Gain	10	Distance above seafloor	0.6 m
Laser intensity	90	Ambient light filtering	On

$$\sigma = \sqrt{\frac{1}{N} \sum_{n=1}^N (S_{n,raw} - \bar{S})^2} = \sqrt{\frac{1}{N} \sum_{n=1}^N S_n^2} = S_q \quad (1)$$

where S is the corrected surface, S_q the standard deviation, \bar{S} the mean value of S , N the total number of measurements, and n the running index (from 1 to N).

The skewness describes the deviation between the measured topography elevation distribution and a normal distribution. The surface skewness defines the asymmetry of the analysed surface. For normally distributed datasets, S_{sk} is 0. Increasing S_{sk} values indicate the dominance of values above the mean, whereas decreasing S_{sk} values correspond to the dominance of values lower than the mean. Applied to the seafloor topography, a high skewness implies an abundance of peaks on the seafloor, whereas a low skewness indicates a dominance of depressions. S_{sk} was calculated by

$$S_{sk} = \frac{\frac{1}{N} \sum_{n=1}^N (S_n - \bar{S})^3}{\left(\sqrt{\frac{1}{N} \sum_{n=1}^N (S_n - \bar{S})^2} \right)^3} \quad (2)$$

where S is the corrected surface, S_{sk} , N the total number of measurements, and n the running index (from 1 to N).

Spectral parameters

Spectral parameters are essential to link 3D surface structures to deterministic or stochastic processes (Thomson and Emery 2014). To avoid spectral leakage during further processing, the edges of $S(y,z)$ were smoothed by applying a cosine shaped taper filter. The seafloor spectral parameters $F(k_y, k_z)$ were computed by the transformation of the surface $S(y,z)$ to the frequency domain using a 2D FFT function, where k_y and k_z are the wave numbers in y and z direction.

To compare the power spectra to data reported in previous work (e.g. Briggs 1989; Briggs and Williams 2002; Lyons et al. 2002), the power spectra were converted to decibel units.

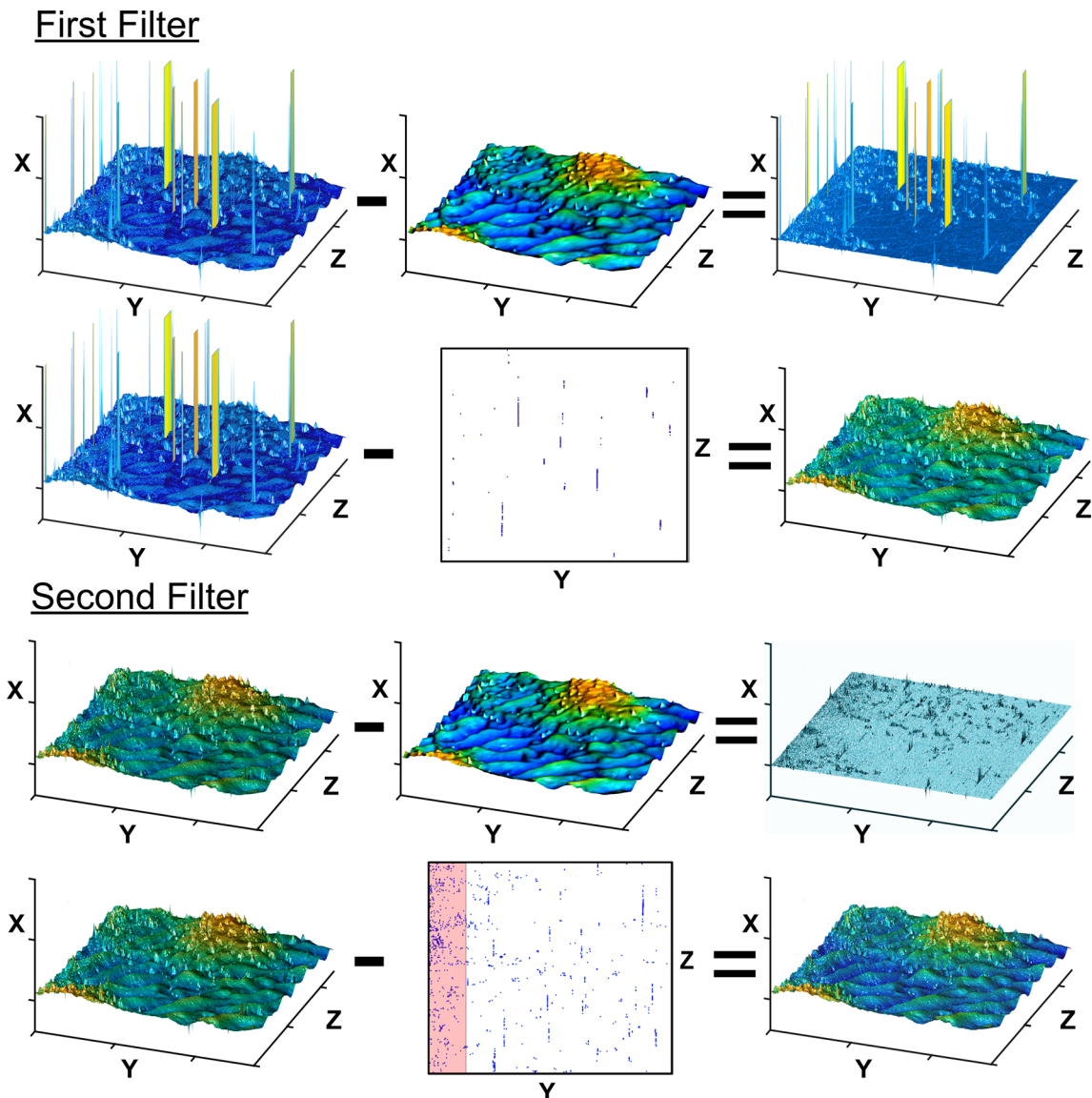


Fig. 3 Schematic representation of removing outliers from raw data. A first filter pass was used to isolate distinct outliers in the water column. A second filter was used to isolate outliers close to the surface. The

increased number of spikes in the area marked red was caused by the increasing angle between the laser and the seafloor. This area was omitted during further processing

The resulting magnitude $M(k_y, k_z)$ of the transformed data $F(k_y, k_z)$ was obtained by

$$M_{k_y, k_z} = 10 \log F_{k_y, k_z}^2 \quad (3)$$

To relate different spatial wavelength intervals to actual microtopography, the filtering method described by Wilken et al. (2012) was adapted. The total spectrum $M(k_y, k_z)$ was subdivided into four different spatial wavelength domains by applying a tapered radial bandpass filter (Fig. 4a–c). The inverse Fourier transformation of the bandpass-filtered spatial wavelength domains revealed the corresponding seafloor topography (Fig. 4, panels A–D).

The actual spatial wavelengths used to define the four spatial wavelength domains (Fig. 4c) were based on measurements of characteristic topographic changes in the digital seafloor model, namely A: 0.1080–0.3600 m (“larger” ripple), B: 0.0400–0.1080 m (“smaller” ripple), C: 0.0155–0.0400 m (transition from macro- to microroughness) and D: 0.0036–0.0155 m (microroughness).

Based on the total power spectrum $M(k_y, k_z)$, a radial average power spectrum (RPS) was calculated by summing the amplitudes for a given spatial wavelength. The summation was performed around semicircles from the origin to account for the symmetry of the 2D FFT spectra. Therefore, to assign specific wave numbers along a radius to the semicircles, a 2D wave vector K was required (Jackson and Richardson 2007):

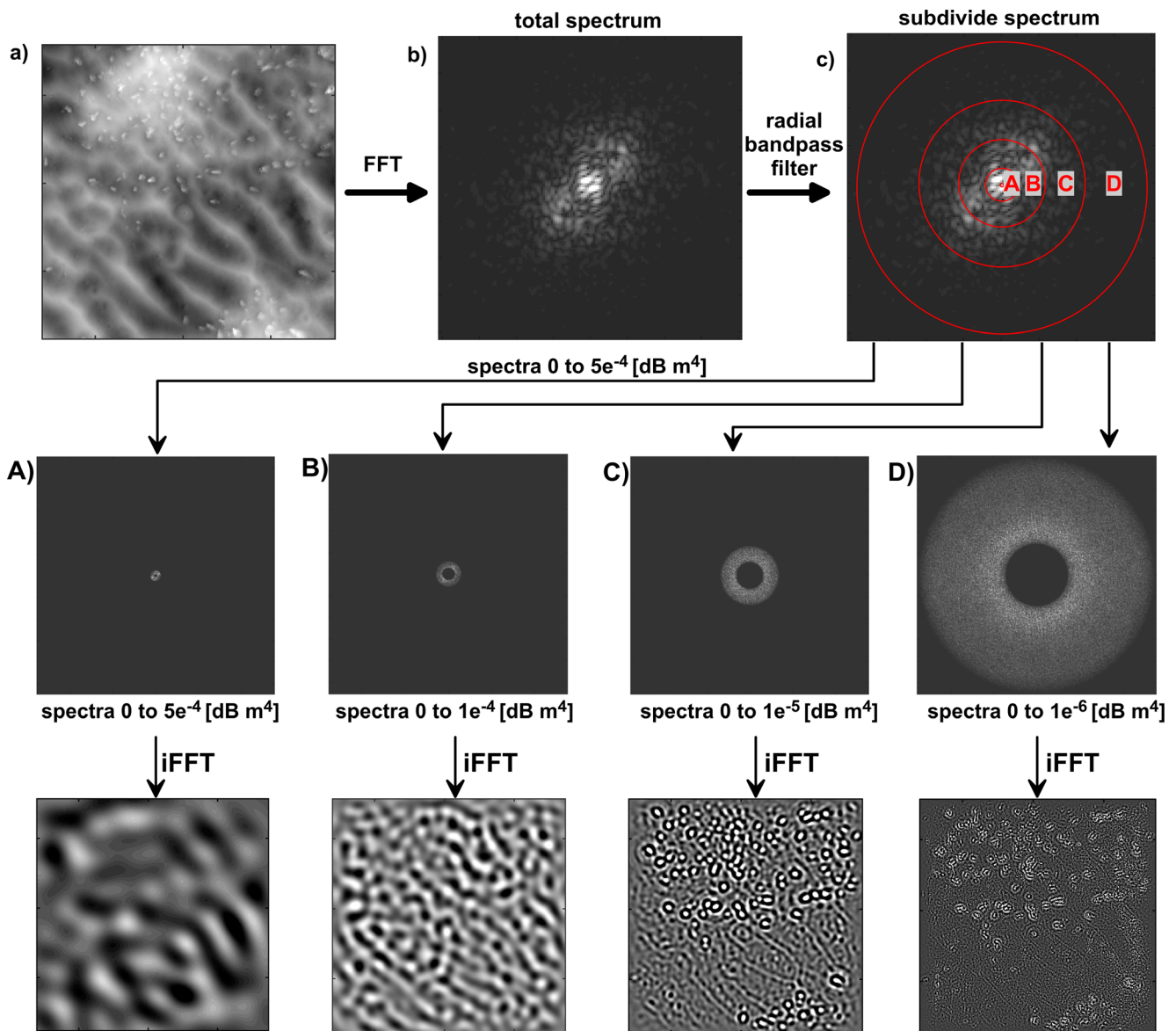


Fig. 4 Schematic overview of the adapted filtering method (cf. Wilken et al. 2012): **a** seafloor model; **b** frequency spectrum of corresponding seafloor model; **c** radial bandpass filter using defined wave numbers to

split the spectrum into four intervals (A–D). The lower images represent the corresponding topography obtained by the inverse Fourier transformation

$$K = \sqrt{k_y^2 + k_z^2} \tag{4}$$

The RPS allows observation of the roughness magnitude of a distinct spatial wavelength over the complete 2D spectrum and thus its contribution to the overall roughness; RPS was calculated by

$$RPS(K) = \frac{1}{N_r(K)} \sum_{n=1}^{N_r(K)} M_n(K) \tag{5}$$

where N_r is the total number of values that lie upon semicircles.

Results

Backscatter strength and underwater video images

The locations for underwater laser deployment (Table 2) were determined by a side scan sonar profile recorded on 20th August 2015 immediately before the microtopography measurements. Side scan data covered $\sim 0.5 \text{ km}^2$ and were recorded using an EdgeTech 4200-MP side scan sonar (300 and 600 kHz). The side scan image was subdivided into a sequence of high and low backscatter strength areas (Fig. 1).

The northernmost laser station 1 was located in an area of high backscatter strengths. Because of the high turbidity at

Table 2 Position and area covered for stations 1 to 3

Station	Lat. (°N)	Long. (°E)	Grid area (m ²)
1	54.9977	8.3104	0.490
2	54.9854	8.3094	0.512
3	54.9772	8.3109	0.503

station 1, the video quality was insufficient to reveal details but still revealed the general, rippled seafloor topography (Fig. 5).

Laser station 2 was located in an approximately 300 m wide stripe of seafloor characterized by low backscatter

strengths. The backscatter data showed a highly chaotic texture at this station. The video snapshot for station 2 (Fig. 5) showed mainly a mix of light green to grey-green shaded smaller ripple structures. Additionally, some dark coloured areas identified as patches of the tubeworm *L. conchilega* existed at the top right and lower right edges, and several light coloured shell fragments were spread over the surface.

The southernmost laser station 3 was located at approximately 500 m from an E–W directed stripe of high backscatter strength. Individual patches of higher backscatter strengths could be recognized in the side scan sonar data. Similar to station 2, the video data at station 3 showed a mix of light

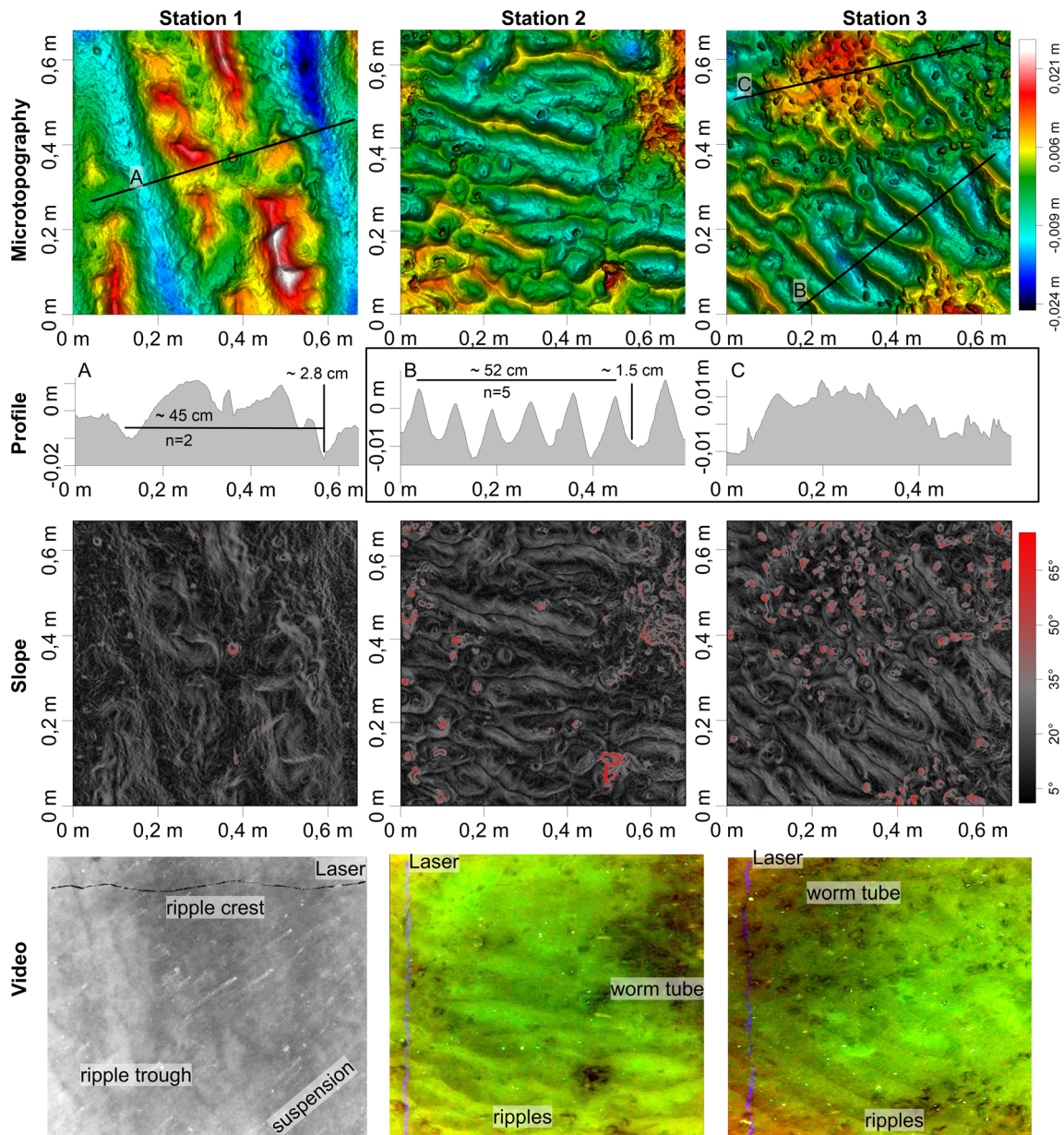


Fig. 5 Overview of the seafloor at the three investigated stations. The video snapshots are distorted. The snapshot of station 1 is plotted in greyscales because of the high suspension load and low contrast

green and grey-green smaller ripple structures. Dark grey macrobenthic patches were visible in the top left and bottom right corners. In contrast to station 2, the *L. conchilega* patches were less dense and more evenly distributed. Few occurrences of other macrobenthos (e.g. ophiuroids, brittle stars) were observed within the rippled seafloor. Small, bright coloured shell fragments were scattered on the seafloor.

Microtopography

Bedforms

The microtopography at laser station 1 showed a well-defined straight ripple structure with superimposed ripples of smaller dimensions (Fig. 5). The ripple crestlines were discontinuous, and the local height distribution was multimodal. At station 2, the microtopography revealed a unidirectional ripple pattern with sharp crestlines. Station 3 showed a unidirectional ripple pattern with sharp crestlines. The elevation distribution of both stations 2 and 3 closely followed a normal distribution

(Fig. 6). Ripple amplitudes, wavelengths and steepness for the three stations are summarized in Table 3.

Biogenic features

At station 1, a circular structure in the centre, a small circular structure at the bottom and a circular structure in the upper right with slopes of $>35^\circ$ were interpreted as being of macrobenthic origin (e.g. polychaetes or endobenthic crustaceans), although the features could not be recognized in the underwater video stills due to heavy suspension at station 1. A high abundance of tube-like structures was observed at stations 2 and 3. The maximum measured height of a single structure was approximately 1.1 cm, although most structures had measured heights of approximately 0.5 cm. The average measured diameter was 0.7–1.4 cm. The measured local slope of the structures ranged from 35° to more than 65° . Tube density varied strongly from single tubes to dense tube patches, with a maximum of 36 tubes in an area of 0.04 m^2 (equivalent to 900 tubes/m^2) at station 3. In total, five tubes

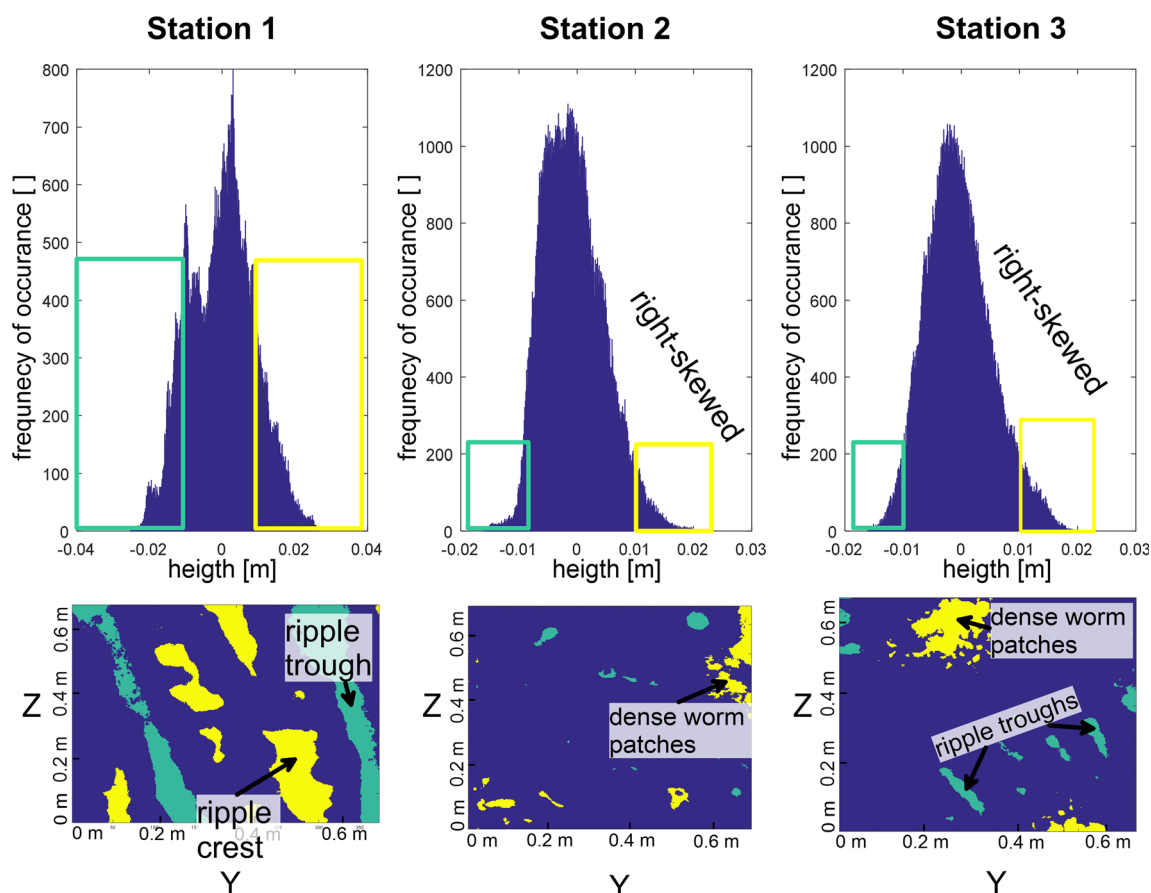


Fig. 6 Histogram of height distribution at stations 1 to 3. Station 1 displays a multimodal distribution. Stations 2 and 3 more closely follow a normal distribution but are slightly right-skewed because of the increased abundance of elevations. The position of these elevations corresponds to the position of the dense tubeworm patches. Yellow and

turquoise boxes mark the areas with significant offsets between a normal Gaussian distribution and the digital height distribution model. Yellow areas values on the right side of the distribution curve representing ripple crests and worm tubes, turquoise areas values on the left side representing topographic depressions

Table 3 Bedform characteristics at stations 1 to 3

Station	Ripple amplitude (m)	Ripple wavelength (m)	Ripple steepness
1	Primary 0.028, secondary 0.010	Primary 0.45, secondary 0.20	Primary 16
2	0.015	0.12	7
3	0.015	0.10	7

were counted at station 1, 60 at station 2 and 115 at station 3. In areas of dense tube cover, the seabed was slightly elevated by up to 1.5 cm above the surrounding seabed, and the ripple pattern was generally less distinct in these areas. The locations of the tube-like structures in the digital elevation model matched those of *L. conchilega* tubes observed by underwater video (Fig. 5).

Amplitude parameters

The amplitude parameters RMS roughness and skewness for the three stations and the filtered spatial wavelength domains are summarized in Fig. 7. The RMS roughness was highest at station 1, although the trend reversed at higher spatial frequencies (spatial wavelength domains B, C and D), where the RMS roughness was higher for stations 2 and 3. The RMS roughness decreased with decreasing spatial wavelength. The skewness was highest for stations 2 and 3, with the right-skewness also observed from the histogram (Fig. 6). The skewness of the height distributions of all stations was mainly caused by increased values in spatial wavelength domain C (all stations) and D (station 3).

Spectral parameters

At all stations, the longest sampled wavelength was 0.3600 m and the shortest sampled wavelength was

0.0036 m because of the grid node spacing of 0.0018 m. The RPS (Fig. 8, top) demonstrates the differences between the three stations. As expected, the roughness magnitude decreased with decreasing spatial wavelength; however, several exceptions were observed. At low wavelengths between 0.36 and 0.04 m (domain A), station 1 had the highest roughness magnitude. This trend was reversed starting at wavelengths below 0.04 m, where the roughness magnitude of stations 2 and 3 exceeded that of station 1 (domain C). The roughness magnitude was similar for stations 2 and 3 down to a wavelength of 0.016 m, whereas at lower spatial wavelengths (domain D) the roughness magnitude of station 3 exceeded that of station 2.

The inverse Fourier transformed microtopography (Fig. 8) demonstrates the topographic elements responsible for the roughness magnitude at different spatial wavelength domains. Within domain A, the roughness magnitude was controlled by large-scale ripple structures at station 1, whereas no structured topographic features existed in the spatial wavelength interval at stations 2 and 3. Within domain B, all three stations displayed complex ripple features. At the transition from domain B to domain C, the roughness magnitude of stations 2 and 3 exceeded that of station 1. The topography of domain C was dominated by ripple structure residuals and the onset of macrobenthic structures at stations 2 and 3. Finally, domain D represented microtopographic

Fig. 7 RMS roughness and surface skewness for the three stations. The domains comprise the complete measured topography (total) and, with decreasing spatial wavelength, the expected spatial wavelength domains A (0.3600–0.1080 m), B (0.1080–0.0400 m), C (0.0400–0.0155 m) and D (0.0155–0.0036 m)

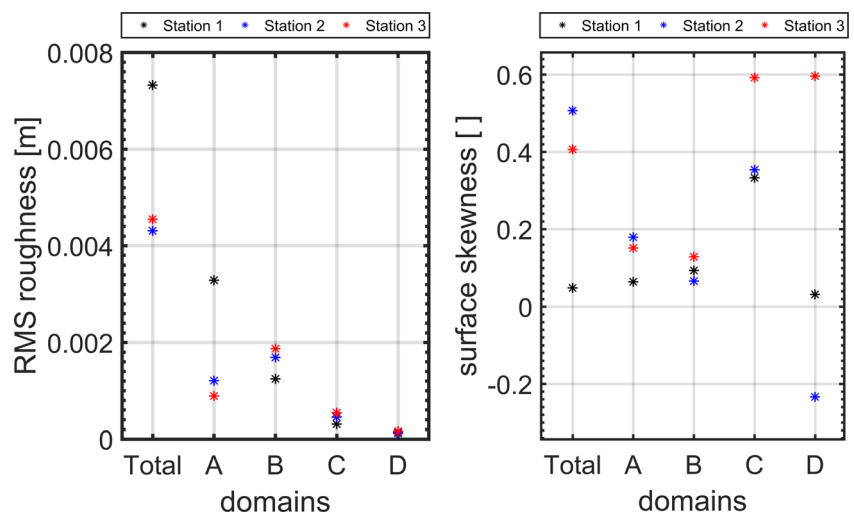
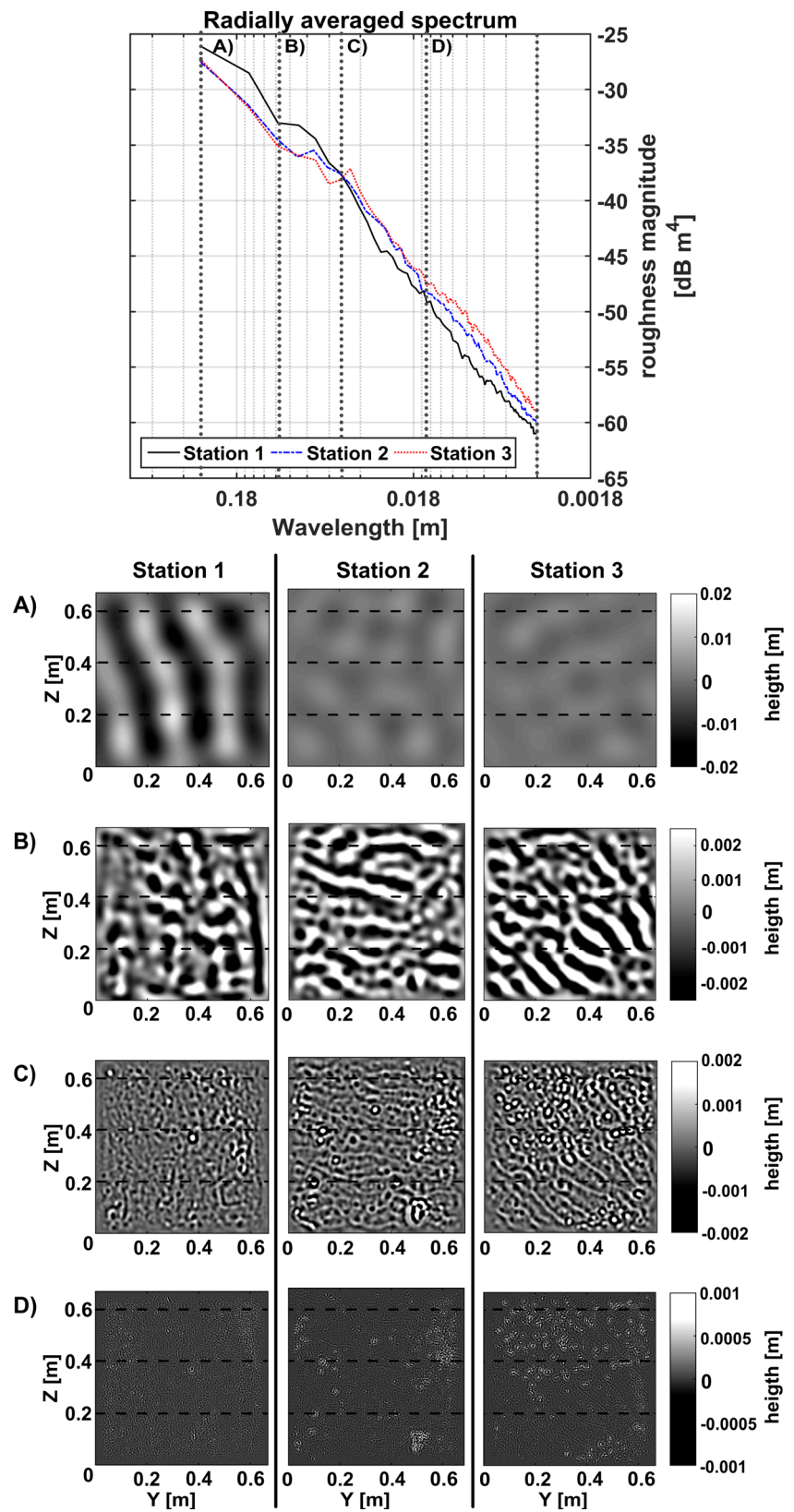


Fig. 8 *Upper panel* Radial power spectrum displaying the roughness magnitude and the spatial wavelength. *Lower panels, A–D* Inverse Fourier transformed topography of the four spatial wavelength domains showing the topographic features that control the roughness magnitude at different spatial wavelengths



structures at spatial wavelengths of less than 1.5 cm. In addition to random microughness elements within the

ripple troughs, the generally observed elevation features of this domain were dominated by worm tubes only.

Discussion

Impact of tubeworms on microtopography

In this study, amplitude and spectral roughness parameters were calculated to determine the morphological fingerprint of tubeworms compared with abiotic seafloor and to test the suitability of morphological parameters for the development of indicator variables. The locations of test sites were selected based on side scan sonar profiles. Because of the extensive ground truthing of previous studies, the recorded backscatter data and underwater videos could be directly related to the general seafloor facies. The E–W directed, rippled patches of high backscatter intensity (station 1) were identified as sorted bedforms (Diesing et al. 2006; Markert et al. 2013; Mielck et al. 2015). The sorted bedforms were surrounded by seafloor composed of fine sand (Mielck et al. 2015), which showed a lighter but chaotic texture in backscatter strength data (stations 2 and 3, Fig. 1) that has been related to the presence of worm tubes (Rattray et al. 2009; Markert et al. 2013; Heinrich et al. 2016).

Tube structures measured with the laser system and identified as *L. conchilega* in accompanying video data are 1.5–3 times larger than the tubes of adult *L. conchilega* (~0.5 cm, Ziegelmeier 1952). Larger diameters in the measured topography data may be caused by (1) a fringe at the top of the worm tube that was measured by the laser line scanner or (2) an inclination of the worm tubes due to, for example, currents, resulting in their tops being less well defined.

The seafloor elevation distribution was dominated by ripples of different wavelengths that appeared at all stations (Fig. 4). The ripples dominated the longer spatial wavelengths and therefore comprised the majority of the roughness magnitude. The ripples at stations 2 and 3 were formed by oscillatory wave movement sand, with a steepness between 4.5 and 7.5, representing wave-induced vortex ripples (Tanner 1967). The ripples at station 1 were composed of coarser sediment and had a steepness of 16, although this value represents a maximum because of the reworking indicated by the fuzzy ripple crestlines. These ripples were likely formed by higher fluid velocities—e.g. during storms able to move sediments within the sorted bedforms (Wiberg and Harris 1994; Murray and Thielert 2004; Bartholdy et al. 2015). Subsequent partial reworking of the ripples under lower energy conditions likely explains the multimodal height distribution only observed at station 1 (Fig. 6).

Despite the dominance of the ripple morphology, the height distribution in areas where tubeworms were present was clearly different from that of hydrodynamic bedforms. The elevated patches (approximately 1.5 cm) beneath dense tubeworm patches at stations 2 and 3 indicate increased local sediment accumulation. Deposited sediment can comprise both mobile sand that is trapped and faecal pellets that, for polychaetes, can

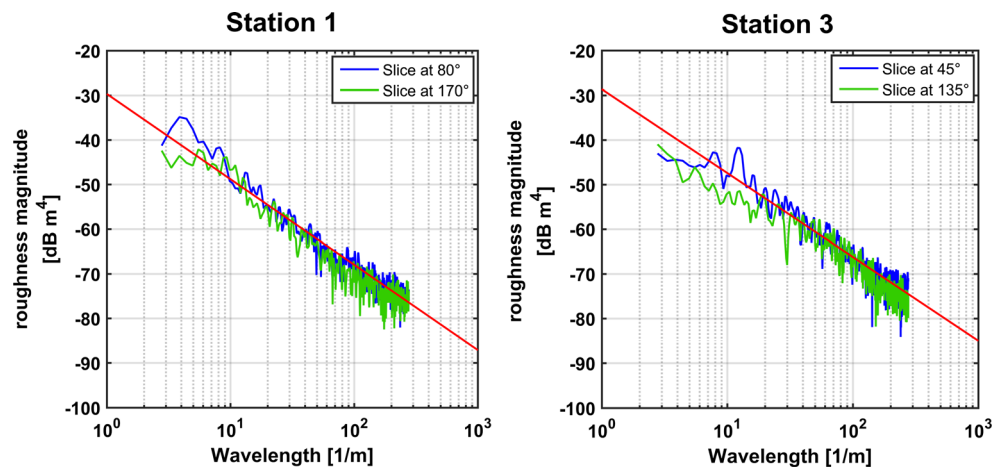
be deposited in close vicinity to the worm (Taghon et al. 1984). Where dense, elevated tubeworm patches were present, the underlying ripple morphology disappeared or became more irregular (Fig. 5). The formation of ripples may have been hindered because of the decrease of near-bottom flow velocity caused by the presence of tubeworms above a certain density threshold (McCall and Tevesz 1982; Eckman 1983). Additionally, the preservation of cohesive faecal pellets held together by microbial mucus in the area of dense worm patches (Nowell et al. 1981; Saba and Steinberg 2012; Kulkarni and Panchang 2015) may have impeded the initiation of ripple formation. No sediment samples were available to determine the cohesiveness of the sediment; however, the video stills showing brownish to blackish colours (Fig. 5) indicating that these sediments were finer with higher organic content compared with the surrounding sandy seafloor that appeared as greenish colours. Because ripples can be continuously formed in the tidal environment at the investigated stations and the tubeworm colonies can be stable over longer periods of time reaching up to several years (McCall and Tevesz 1982)—depending on the occurrence of extreme events (Heinrich et al. 2016)—the reworking of existing ripples due to biological action (Soulsby et al. 2012) is considered to be of less importance in the study area.

In addition to the larger-scale impact on the mean elevation heights by accumulated sediment, the impact of the tubeworms themselves on the local height distribution could be observed. The increased probability of high elevation values compared with a normal distribution explains the slight skewness to the right (Figs. 5 and 6). The notion that the skewness was induced by the worm tubes—and not by, for example, the observed ripples—was confirmed by plotting the location of the elevation values of the right-skewed part of the histogram between 0.012 and 0.016 cm (Fig. 6). These values coincided with the locations of dense tubeworms in video and bathymetric data. This showed that the increased probability of elevations compared with a normal distribution was caused exclusively by individual worm tubes within the available data.

Although notable in histograms based on the complete measured topography as discussed above, the impact of tubeworms on microtopography was concentrated to shorter spatial wavelengths within domains C and D. In these domains, the RMS roughness and roughness magnitude at stations 2 and 3 were slightly increased compared with station 1 and the worms were clearly recognized within the bandpass-filtered topography (Figs. 6 and 7). Interestingly, albeit with two stations having a very limited dataset, the increase of tubeworm occurrences from 60 to 115 between stations 2 and 3 enhanced only the magnitude of roughness and not the spatial wavelength interval impacted by the tubeworms.

Seafloor roughness magnitude spectra are frequently described by power-law dependencies of the form $M(K) = \omega/$

Fig. 9 Profiles showing the decay of roughness magnitude along two profiles normal (*blue lines*) and parallel (*green lines*) to the observed ripples at stations 1 and 3. The red lines represent a spectral exponent of -1.9 for both stations 1 and 3. The norm of the residuals is approximately 50 for station 1 and 58 for station 3



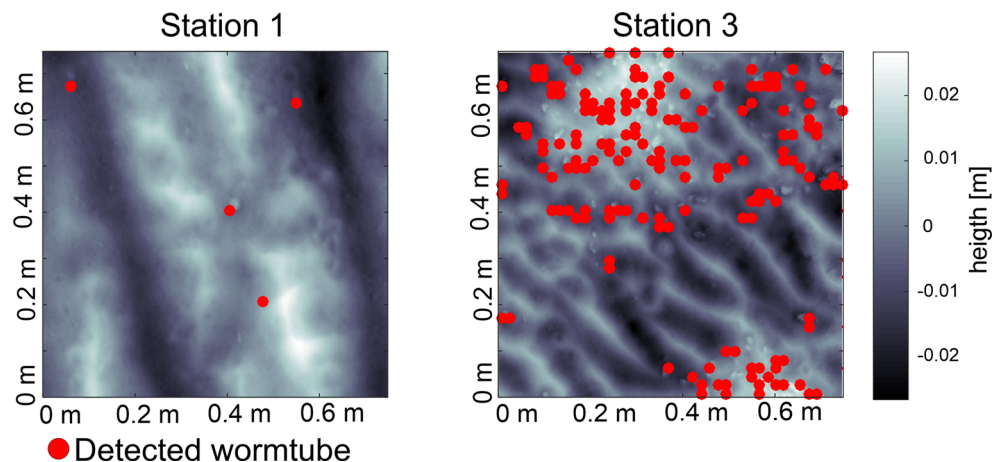
K^γ , where $M(K)$ is the roughness spatial spectrum, ω is the spectral strength and γ is the spectral exponent (Jackson and Richardson 2007). Therefore, the spectral exponent equals the slope of a linear approximation of the roughness spectrum displayed in a log–log plot (in the present case, divided by 10 to account for the multiplication of $M(K)$ by 10). It is commonly assumed that the description of roughness magnitude spectra by power laws is valid over a wide range of scales, and spectral exponents between -1.5 and -3.5 have been reported (Lyons et al. 2002; Jackson and Richardson 2007; Jackson et al. 2009). However, it is poorly known if these spectral exponents are valid for high spatial wave numbers and/or biologically impacted seafloor. Since the RPS and the bandpass-filtered topography (Fig. 8) show an increase of roughness magnitude at shorter spatial wavelengths in domains C and D, a deviation from power law behaviour caused by local macrobenthos may be expected for this interval. Available power laws are typically determined from 1D profiles or slices through 2D spectra (Briggs et al. 2005). Slices across and parallel to the ripple direction through the spectra of stations 1 and 3 are shown in Fig. 9. The impact of ripples at both stations can be clearly observed in domains A and B

between the profiles normal and parallel to the ripple direction. The differences observed in domains C and D were minor. Although slightly higher roughness magnitudes were present within domain C and at the onset of domain D, these changes were insignificant (Fig. 9). Because the impact of macrobenthos was clearly observed in the RPS and bandpass-filtered topography (Fig. 8), the use of roughness magnitude profiles derived from 1D profiles and slices of 2D data appears insufficient to capture the impact of macrobenthos on seafloor roughness characteristics.

Implications for the identification of tubeworms by remote sensing

The contrast between hydrodynamic and biological microtopography height distributions, with hydrodynamic processes causing both elevations and depressions and benthic organisms causing preferably steeper elevations, opens up the use of height distribution data for seafloor classification. A simple example is the use of height distribution, skewness and slope over small subsets of the complete bathymetric data. Although the skewness for the complete microtopography

Fig. 10 Areas in the elevation model where a 9×9 grid subset was characterized by a maximum slope of $>40^\circ$ and a skewness of >0.5 (*red dots*). Worm tubes are reliably tracked with only few outliers (e.g. the lowermost detection at station 1)



measured at station 2 was lower at long spatial wavelengths compared with station 1 (Fig. 8), it is assumed that this was caused by the low tubeworm density and that individual tubeworms still increased the local skewness. This was also indicated by the high skewness (>0.5) observed at short spatial wavelengths for station 3, which was dominated by tubeworms (Fig. 7). The measured slope of the tubeworms was found to be in excess of 35° (Fig. 5), clearly exceeding the angle of repose for rippled angular and round sand (Miller and Byrne 1966). Figure 10 presents an example where image skewness was calculated over 9×9 grid node subsets of the complete topographic data, corresponding to a square of 0.0162×0.0162 m, thus covering the diameter of a typical observed tubeworm and adjacent seafloor. A skewness threshold of 0.5 and, considering that the angle of repose may be considerably higher for poorly sorted aggregations of grains (Miller and Byrne 1966), a slope threshold of 40° were used for classification purposes. The results show that most, but not all, worm tubes were captured reliably (Fig. 10), and confusion with hydrodynamic features was rare. It remains to be investigated whether a reliable detection of tubeworm presence can be achieved using state-of-the-art ship-based (in shallow waters) or towed/AUV-based multibeam or optical systems.

The differences in spatial roughness spectra between hydrodynamic and biological seafloor types may also have implications for the monitoring of tubeworms by methods depending on acoustic backscatter, widespread in today's habitat mapping (Brown et al. 2011). The tubeworms consist of agglutinated sand grains (Ziegelmeir 1952), and their material may thus be approximated as having an acoustic impedance contrast to water similar to that of the seafloor not covered by worm tubes. Generally, seafloor roughness increases with tubeworm density, as was demonstrated by RMS roughness. The tubes impact a specific part of the roughness spectrum with spatial wavelengths between 0.0200 and 0.0036 m, corresponding to sound frequencies of 75 and 400 kHz, which are commonly used for acoustic monitoring purposes. In fact, Heinrich et al. (2016) recently reported first indications that *L. conchilega* patches of different population densities can be differentiated based on side scan sonar backscatter strength data recorded at 200 kHz.

Conclusions

Using an underwater laser line scanner, three areas of approximately 0.5 m^2 each were mapped with mm accuracy in highly turbid waters. The resulting datasets served to delineate the impact of tubeworms on seafloor microtopography. The impacts were characterized by (1) a 1.5 cm accumulation of sediment in the vicinity of dense tubeworm patches and (2) increased slope, skewness and root mean square roughness at

short spatial wavelengths between 0.0200 and 0.0036 m. It was shown that the deviation of seafloor roughness magnitudes from a pure power law behaviour caused by the presence of tubeworms could only be detected when the complete spectrum was considered, whereas 1D profiles were insufficient. The local slope and skewness changes were used to construct a simple classification algorithm that tracked tubeworm occurrence. The limitation of the roughness changes induced by tubeworms for specific spatial wavelengths may improve their detection in acoustic scatter data in the future.

Acknowledgements This project was funded by the Cluster of Excellence 80 “The Future Ocean” within the framework of the Excellence Initiative by the Deutsche Forschungsgemeinschaft (DFG) on behalf of the German federal and state governments. The helpful comments of one reviewer and the editors are highly appreciated. Special thanks go to Heiko Jähmlich for building the underwater frame and housings, and to the crew of Mya II (AWI) for their assistance during the fieldwork. We thank Thomas Meier and Klaus Schwarzer for valuable comments and Björn Peiler for his assistance with C/C++ programming.

Compliance with ethical standards

Conflict of interest The authors declare that there is no conflict of interest with third parties.

References

- Anderson JT, Van Holliday D, Kloser R, Reid DG, Simard Y (2008) Acoustic seabed classification: current practice and future directions. *ICES J Mar Sci* 65:1004–1011. doi:10.1093/icesjms/fsn061
- Armonies W (2000) On the spatial scale needed for benthos community monitoring in the coastal North Sea. *J Sea Res* 43:121–133. doi:10.1016/S1385-1101(00)00008-3
- Bartholdy J, Ernstsen VB, Flemming BW, Winter C, Bartholomä A, Kroon A (2015) On the formation of current ripples. *Sci Rep* 5: 11390. doi:10.1038/srep11390
- Bhushan B (2001) *Modern tribology handbook*. CRC Press, Boca Raton
- Briggs KB (1989) Microtopographical roughness of shallow-water continental shelves. *IEEE J Ocean Eng* 14:360–367. doi:10.1109/48.35986
- Briggs KB, Williams KL (2002) Characterization of interface roughness of rippled sand off Fort Walton Beach, Florida. *IEEE J Ocean Eng* 27:505–514. doi:10.1109/JOE.2002.1040934
- Briggs KB, Lyons AP, Pouliquen E (2005) Seafloor roughness, sediment grain size, and temporal stability. In: *Proc Int Conf Underwater Acoustic Measurements: Technologies & Results*, Heraklion, Crete, pp 337–343
- Brown CJ, Collier JS (2008) Mapping benthic habitat in regions of gradational substrata: an automated approach utilising geophysical, geological, and biological relationships. *Estuar Coast Shelf Sci* 78: 203–214. doi:10.1016/j.ecss.2007.11.026
- Brown CJ, Smith SJ, Lawton P, Anderson JT (2011) Benthic habitat mapping: a review of progress towards improved understanding of the spatial ecology of the seafloor using acoustic techniques. *Estuar Coast Shelf Sci* 92:502–520. doi:10.1016/j.ecss.2011.02.007
- Che H-R, Ierodiaconou D, Laurenson L (2012) Combining angular response classification and backscatter imagery segmentation for

- benthic biological habitat mapping. *Estuar Coast Shelf Sci* 97:1–9. doi:10.1016/j.ecss.2011.10.004
- Coggan R, Diesing M (2011) The seabed habitats of the central English Channel: a generation on from Holme and Cabioch, how do their interpretations match-up to modern mapping techniques? *Cont Shelf Res* 31:132–150. doi:10.1016/j.csr.2009.12.002
- Diesing M, Stephens D (2015) A multi-model ensemble approach to seabed mapping. *J Sea Res* 100:62–69. doi:10.1016/j.seares.2014.10.013
- Diesing M, Kubicki A, Winter C, Schwarzer K (2006) Decadal scale stability of sorted bedforms, German Bight, southeastern North Sea. *Cont Shelf Res* 26:902–916. doi:10.1016/j.csr.2006.02.009
- Diesing M, Green SL, Stephens D, Lark RM, Stewart HA, Dove D (2014) Mapping seabed sediments: comparison of manual, geostatistical, object-based image analysis and machine learning approaches. *Cont Shelf Res* 84:107–119. doi:10.1016/j.csr.2014.05.004
- Eckman J (1983) Hydrodynamic processes affecting benthic recruitment. *Limnol Oceanogr* 28:241–257
- European Parliament, European Council (2008) Establishing a framework for community action in the field of marine environmental policy (Marine Strategy Framework Directive). Official Journal of the European Union, vol 164, pp 19–40
- Heinrich C, Feldens P, Schwarzer K (2016) Highly dynamic biological seabed alterations revealed by side scan sonar tracking of *Lanice conchilega* beds offshore the island of Sylt (German Bight). *Geo-Mar Lett*. doi:10.1007/s00367-016-0477-z
- Jackson D, Richardson M (2007) High-frequency seafloor acoustics. Springer, Heidelberg. doi:10.1007/978-0387-36945-7
- Jackson DR, Richardson MD, Williams KL, Lyons AP, Jones CD, Briggs KB, Tang D (2009) Acoustic observation of the time dependence of the roughness of sandy seafloors. *IEEE J Ocean Eng* 34:407–422
- Kulkarni KG, Panchang R (2015) New insights into polychaete traces and fecal pellets: another complex ichnotaxon? *PLoS ONE* 10:e0139933. doi:10.1371/journal.pone.0139933
- Lefebvre A, Ernsten VB, Winter C (2011) Bedform characterization through 2D spectral analysis. *J Coast Res* 64:781–785
- Lefebvre A, Ernsten VB, Winter C (2013) Estimation of roughness lengths and flow separation over compound bedforms in a natural-tidal inlet. *Cont Shelf Res* 61–62:1–14. doi:10.1016/j.csr.2013.04.030
- Leys C, Ley C, Klein O, Bernard P, Licata L (2013) Detecting outliers: do not use standard deviation around the mean, use absolute deviation around the median. *J Exp Soc Psychol* 49:764–766. doi:10.1016/j.jesp.2013.03.013
- Lyons AP, Fox WLJ, Hasiotis T, Pouliquen E (2002) Characterization of the two-dimensional roughness of wave-rippled sea floors using digital photogrammetry. *IEEE J Ocean Eng* 27:515–524. doi:10.1109/JOE.2002.1040935
- Maki T, Kume A, Ura T (2011) Volumetric mapping of tubeworm colonies in Kagoshima Bay through autonomous robotic surveys. *Deep Sea Res I Oceanogr Res Pap* 58:757–767. doi:10.1016/j.dsr.2011.05.006
- Markert E, Holler P, Kröncke I, Bartholomä A (2013) Benthic habitat mapping of sorted bedforms using hydroacoustic and ground-truthing methods in a coastal area of the German Bight/North Sea. *Estuar Coast Shelf Sci* 129:94–104. doi:10.1016/j.ecss.2013.05.027
- McCall P, Tevesz ML (1982) Animal-sediment relations: the biogenic alteration of sediments. *Topics in Geobiology*, vol 100. Springer, Heidelberg
- Mielck F, Holler P, Bürk D, Hass HC (2015) Interannual variability of sorted bedforms in the coastal German Bight (SE North Sea). *Cont Shelf Res* 111(A):31–41. doi:10.1016/j.csr.2015.10.016
- Miller RL, Byrne RJ (1966) The angle of repose for a single grain on a fixed rough bed. *Sedimentology* 6:303–314. doi:10.1111/j.1365-3091.1966.tb01897.x
- Moore KD, Jaffe JS (2002) Time-evolution of high-resolution topographic measurements of the seafloor using a 3-D laser line scan mapping system. *IEEE J Ocean Eng* 27:525–545. doi:10.1109/JOE.2002.806304
- Murray AB, Thiel ER (2004) A new hypothesis and exploratory model for the formation of large-scale inner-shelf sediment sorting and rippled scour depressions. *Cont Shelf Res* 24:295–315. doi:10.1016/j.csr.2003.11.001
- Nowell ARM, Jumars PA, Eckman JE (1981) Effects of biological activity on the entrainment of marine sediments. *Mar Geol* 42:133–153
- Pouliquen E, Lyons AP (2002) Backscattering from bioturbated sediments at very high frequency. *IEEE J Ocean Eng* 27:388–402. doi:10.1109/JOE.2002.1040926
- Rattray A, Ierodiaconou D, Laurenson L, Burq S, Reston M (2009) Hydro-acoustic remote sensing of benthic biological communities on the shallow South East Australian continental shelf. *Estuar Coast Shelf Sci* 84(2):237–245
- Saba GK, Steinberg DK (2012) Abundance, composition, and sinking rates of fish fecal pellets in the Santa Barbara Channel. *Sci Rep* 2:716. doi:10.1038/srep00716
- Soulsby RL, Whitehouse RJS, Marten KV (2012) Prediction of time-evolving sand ripples in shelf seas. *Cont Shelf Res* 38:47–62. doi:10.1016/j.csr.2012.02.016
- Taghon GL, Nowell ARM, Jumars PA (1984) Transport and breakdown of fecal pellets: biological and sedimentological consequences. *Limnol Oceanogr* 29:64–72. doi:10.4319/lo.1984.29.1.0064
- Tanner WF (1967) Ripple mark indices and their uses. *Sedimentology* 9:89–104. doi:10.1111/j.1365-3091.1967.tb01332.x
- Thomson RE, Emery WJ (2014) Data analysis methods in physical oceanography, 3rd edn. Elsevier, Amsterdam
- Tillmann T, Wunderlich J (2011) Facies and development of a Holocene barrier spit (southern Sylt/German North Sea). In: 6th Int Workshop Advanced Ground Penetrating Radar (IWAGPR), pp 1–7. doi:10.1109/IWAGPR.2011.5963874
- Wang C-C, Tang D (2012) Application of underwater laser scanning for seafloor shell fragments characterization. *J Mar Sci Technol* 20:95–102. <http://jmst.ntou.edu.tw/marine/20-1/95-102.pdf>
- Wiberg PL, Harris CK (1994) Ripple geometry in wave-dominated environments. *J Geophys Res* 99:775–789. doi:10.1029/93JC02726
- Wilken D, Feldens P, Wunderlich T, Heinrich C (2012) Application of 2D Fourier filtering for elimination of stripe noise in side-scan sonar mosaics. *Geo-Mar Lett* 32:337–347. doi:10.1007/s00367-012-0293-z
- Zeiler M, Schulz-Ohlberg J, Figge K (2000) Mobile sand deposits and shoreface sediment dynamics in the inner German Bight (North Sea). *Mar Geol* 170:363–380. doi:10.1016/S0025-3227(00)00089-X
- Ziegelmeier E (1952) Beobachtungen über den Röhrenbau von *Lanice conchilega* (Pallas) im Experiment und am natürlichen Standort. *Helgoländer Meeresun* 4:107–129. doi:10.1007/BF02178540